The Formation of a Massive Galaxy Cluster Core at $z = 4.3$

T. B. Miller[1,2,*], S. C. Chapman[1,3], M. Aravena[4], M. L. N. Ashby[5], C. C. Hayward[5,6], J. D. Vieira[7], A. Weiß[8], A. Babul[9], M. Béthermin[10], C. M. Bradford[11,12], M. Brodwin[13], J. E. Carlstrom[14,15,16,17], Chian-Chou Chen[18], D. J. M. Cunningham[1,19], C. De Breuck [18], A. H. Gonzalez[20], T. R. Greve[21], Y. Hezaveh[22], K. Lacaille[1,23], K. C. Litke[24], J. Ma[20], M. Malkan[25], D. P. Marrone[24], W. Morningstar[22], E. J. Murphy[26], D. Narayanan[20], E. Pass[1,27], R. Perry[1], K. A. Phadke[7], K. M. Rotermund[1], J. Simpson[28,29], J. S. Spilker[24], J. Sreevani[7], A. A. Stark[5], M. L. Strandet[8,30] & A. L. Strom[31]

[1]Department of Physics and Atmospheric Science, Dalhousie University, Halifax, Canada
[2]Department of Astronomy, Yale University, 52 Hillhouse Avenue, New Haven, CT 06511, USA
[3]Institute of Astronomy, Madingley Road, Cambridge CB3 0HA, UK
[4]Núcleo de Astronomía, Facultad de Ingeniería y Ciencias, Universidad Diego Portales, Av. Ejercito 441, Santiago, Chile
[5]Harvard-Smithsonian Center for Astrophysics, 60 Garden Street, Cambridge, MA 02138, USA
[6]Center for Computational Astrophysics, Flatiron Institute, 162 Fifth Avenue, New York, NY 10010, USA
[7]Department of Astronomy, University of Illinois, 1002 West Green Street, Urbana, IL 61801, USA
[8]Max-Planck-Institut fur Radioastronomie, Auf dem Hügel 69 D-53121 Bonn, Germany
[9]Department of Physics and Astronomy, University of Victoria, Victoria, BC V8P 1A1, Canada
[10]Aix-Marseille Université, CNRS, LAM, Laboratoire d'Astrophysique de Marseille, Marseille, France
[11]California Institute of Technology, 1200 E. California Boulevard, Pasadena, CA 91125, USA
[12]Jet Propulsion Laboratory, 4800 Oak Grove Drive, Pasadena, CA 91109, USA
[13]Department of Physics and Astronomy, University of Missouri, 5110 Rockhill Road, Kansas City, MO 64110, USA
[14] Kavli Institute for Cosmological Physics, University of Chicago, 5640 South Ellis Avenue, Chicago, IL 60637, USA
[15]Department of Physics, University of Chicago, 5640 South Ellis Avenue, Chicago, IL 60637, USA
[16]Enrico Fermi Institute, University of Chicago, 5640 South Ellis Avenue, Chicago, IL 60637, USA
[17]Department of Astronomy and Astrophysics, University of Chicago, 5640 South Ellis Avenue, Chicago, IL 60637, USA
[18]European Southern Observatory, Karl Schwarzschild Straße 2, 85748 Garching, Germany
[19]Department of Astronomy and Physics, Saint Mary's University, Halifax, Nova Scotia, Canada
[20]Department of Astronomy, University of Florida, Bryant Space Sciences Center, Gainesville, FL 32611, USA
[21]Department of Physics and Astronomy, University College London, Gower Street, London WC1E 6BT, UK
[22]Kavli Institute for Particle Astrophysics and Cosmology, Stanford University, Stanford, CA 94305, USA
[23]Department of Physics and Astronomy, McMaster University, Hamilton, ON L8S4M1, Canada
[24]Steward Observatory, University of Arizona, 933 North Cherry Avenue, Tucson, AZ 85721, USA
[25]Department of Physics and Astronomy, University of California, Los Angeles, CA 90095, USA
[26]National Radio Astronomy Observatory, 520 Edgemont Road, Charlottesville, VA 22903, USA
[27]Department of Physics and Astronomy, University of Waterloo, 200 University Avenue West, Waterloo, ON N2L 3G1, Canada
[28]Institute for Astronomy, University of Edinburgh, Royal Observatory, Blackford Hill, Edinburgh EH9 3HJ, UK
[29]Centre for Extragalactic Astronomy, Department of Physics, Durham University, South Road, Durham DH1 3LE, UK
[30]International Max Planck Research School (IMPRS) for Astronomy and Astrophysics, Universities of Bonn and Cologne, Germany
[31]Observatories of The Carnegie Institution for Science, 813 Santa Barbara Street, Pasadena, CA 91101, USA

Massive galaxy clusters are now found as early as ~ 3 billion years after the Big Bang, containing stars that formed at even earlier epochs.[1–3] The high-redshift progenitors of these galaxy clusters, termed 'protoclusters', are identified in cosmological simulations with the highest dark matter overdensities.[4–6]

While their observational signatures are less well defined compared to virialized clusters with a substantial hot intra-cluster medium (ICM), protoclusters are expected to contain extremely massive galaxies that can be observed as luminous starbursts.[7] Recent claimed detections of protoclusters hosting such starbursts[8–11] do not support the kind of rapid cluster core formation expected in simulations[12] because these structures contain only a handful of starbursting galaxies spread throughout a broad structure, with poor evidence for eventual collapse into a protocluster. Here we report that the source SPT2349-56 consists of at least 14 gas-rich galaxies all lying at z = 4.31 based on sensitive observations of carbon monoxide and ionized carbon. We demonstrate that each of these galaxies is forming stars between 50 and 1000 times faster than our own Milky Way, and all are located within a projected region only ~ 130 kiloparsecs in diameter. This galaxy surface density is more than 10 times the average blank field value (integrated over all redshifts) and $>$1000 times the average field volume density. The velocity dispersion (~ 410 km s^{-1}) of these galaxies and enormous gas and star formation densities suggest that this system represents a galaxy cluster core at an advanced stage of formation when the Universe was only 1.4 billion years old. A comparison with other known protoclusters at high redshifts shows that SPT2349-56 is a uniquely massive and dense system that could be building one of the most massive structures in the Universe today.

In a multi-band survey over 2500 deg^2 of sky, the South Pole Telescope (SPT) discovered a population of rare ($n \sim 0.04$ deg^{-2}), extremely bright ($S_{1.4\,\mathrm{mm}} > 20\,$mJy) millimeter-selected sources.[13,14] The Atacama Large Millimeter Array (ALMA) 870-μm imaging showed that more than 90% of these SPT-selected sources are single high-redshift submillimeter galaxies (SMGs)[15] with intrinsic flux densities of $S_{870\,\mu\mathrm{m}} = 5 - 10\,$mJy, but gravitationally lensed by factors of $5 - 20$,[16] with a median redshift $z \sim 4$.[17] However, $\sim 10\%$ of these sources show no evidence for lensing and may instead be intrinsically very luminous galaxies or even groups of multiple rapidly star-forming galaxies. The brightest such source in the SPT 2500 deg^2 survey, SPT2349-56 ($S_{1.4\,\mathrm{mm}}$=23.3 mJy), is revealed by LABOCA (a low resolution bolometer camera on the APEX telescope) observations at 870 μm to consist of two elongated sources with a combined flux density $S_{870\,\mu\mathrm{m}} \sim 110\,$mJy (Fig. 1), with the brighter southern source comprising $\sim 77\,$mJy of this flux density. An ALMA redshift survey[17] further resolved SPT2349-56 into a pair of bright 3-mm sources associated with the southern LABOCA source, with both lying at $z = 4.3$.

To better understand the nature of this structure, deep ALMA spectral imaging of the brighter southern peak of the extended LABOCA source was undertaken. A 358-GHz map containing the redshifted [CII]$_{1900.5\,\mathrm{GHz}}$ line was used to search for line-emitting galaxies. A blind spectral line survey (described in the Methods) was performed on the data cube, revealing 14 $z \sim 4.31$ line emitters at high significance (SNR $>$7). Twelve of these emitters are individually detected in the 1.1-mm continuum map at $> 5\sigma$, with 1.1-mm flux densities ranging from 0.2-5 mJy (Fig. 1). The remaining two line emitters (M,N) are both detected at lower significance in the 1.1-mm continuum map but have robust IRAC infrared counterparts (Extended Data Table 1, Extended Data Fig. 4). Nine of these sources are also detected ($> 5\sigma$) in the CO(4-3) line. The ALMA spectra are shown in Fig. 1.

The measurements of both the continuum and spectral lines of the 14 galaxies allow us to estimate their star formation rates (SFRs), gas masses, and dynamical masses (Tables 1 & Extended Data Table 1). The physical properties of these sources indicate that this protocluster already harbors massive galaxies that are rapidly forming stars from an abundant gas supply. The two brightest sources, A & B, have SFRs in excess of 1000 solar masses per year within their resolved $\sim$ 3-kpc radii (Extended Data Table). The total SFR of the 14 sources is 6000 ± 600 $M_\odot$ yr^{-1}. Multi-colour imaging with Herschel-SPIRE (250, 350, 500 μm), in addition to the 870-μm LABOCA map, shows that the northern LABOCA structure is also consistent with lying at $z = 4.3$ (see Methods). The sources detected in the ALMA 870-μm imaging therefore comprise just 50% of the total flux density of the southern LABOCA source and 36% of the total LABOCA flux density, suggesting that the inner ~ 500 kpc of this protocluster contains 16,500 $M_\odot$ $yr^{-1}$of star formation. Modelling the spectral energy distribution based on this combined submillimeter photometry yields an IR luminosity (from 8-1100 μm) of $(8.0 \pm 1.0) \times 10^{13}$ $L_\odot$.

The gas masses of the 14 protocluster galaxies, estimated from CO(4-3), or [CII] if undetected in CO(4-3) (see Methods), range from 1×10^{10} to $1 \times 10^{11} M_\odot$, with a total gas mass of $\sim 6 \times 10^{11}$ $(X_{CO}/0.8)$ $M_\odot$. A follow-up survey of colder molecular gas in CO(2-1) with the ATCA radio telescope detects the bulk of this large gas repository, especially in the central region near sources B, C, & G, and confirms that the assumptions about gas excitation used to convert CO(4-3) to H_2 gas masses of the galaxies are reasonable. Based on simulations[18] and measurements of lower-redshift systems that have a similar gravitational potential well depth, we expect and calculate explicitly in the Methods that the cold gas may comprise only a small fraction of the baryon budget. The bulk of the baryons may already be in the form of a diffuse, hot gas filling the space between the galaxies – the ICM that is characteristic of massive virialized galaxy clusters at $z < 1.5$.

The detected ALMA sources also enable an initial estimate of the mass of the protocluster. We determine the mean redshift using the biweight estimator[19] as $\langle z \rangle_{\rm bi} = 4.3040^{+0.0020}_{-0.0019}$. The velocity dispersion of the galaxy distribution is $\sigma_{\rm bi} = 408^{+82}_{-56}$ km s^{-1} according to the biweight method,[19] which is the standard approach for galaxy samples of this size. Other common methods (gapper,[19] Gaussian fit) agree to within 3% and provide similar errors. Under the assumption that SPT2349-56 is approximately virialized, the mass-dispersion relation for galaxy clusters[20] indicates a dynamical mass of $M_{\rm dyn} = (1.16 \pm 0.70) \times 10^{13}$ $M_\odot$, which is an upper limit if the system has not yet virialized. The total halo mass indicates that the protocluster is a viable progenitor of a $> 10^{15}$ $M_\odot$ galaxy cluster comparable to the Coma cluster at $z = 0$ (Fig. 2).[12] The location of SPT2349-56 in this plane suggests a very massive descendant, but we caution that N-body simulations indicate that it is difficult to reliably predict $z = 0$ halo mass from the halo mass at a given epoch due to the large halo-to-halo variation in dark matter halo growth histories.[21]

To study the relative overdensity and concentration of SPT2349-56, it is desirable to compare with other active protoclusters at high redshift. SPT2349-56 is highly overdense, as it harbors 10 SMGs with $S_{1.1\,\mathrm{mm}} \gtrsim 0.5$ (a level at which we are complete, with uniform sensitivity across our search area) located within a circle of diameter 19″ (130 kpc), corresponding to a number density of $N(S_{1.1\,\mathrm{mm}} > 0.5\,\mathrm{mJy}) \approx 2 \times 10^4$ deg^{-2}. By comparison, the average number of field sources with $S_{1.1\,\mathrm{mm}} > 0.5\,\mathrm{mJy}$ within this area across all redshifts is less than one;[22] thus, this field is overdense by more than a factor of 10. When we account for the fact that all sources are at the same redshift, the volume density is $> 1000\times$ the field density, assuming a redshift binning of Δz=0.1 and the redshift distribution for SMGs.[23] In Fig. 2, we plot 'curves of growth' of the total 870-μm flux density versus on-sky area for SPT2349-56 and other SMG-rich protoclusters (see Methods for the details of the comparison sample). For SPT2349-56, we plot both the total flux density of the 14 confirmed protocluster members detected with ALMA and the total flux density of the extended LABOCA structure. The curve of growth for SPT2349-56 rises much more steeply than those of the other high-redshift protoclusters, demonstrating its extreme density. For SPT2349-56 the on-sky area encompassing the accumulated 870-μm flux density (and thus approximately the total SFR) is as much as 3 orders of magnitude less than for other protoclusters at $z > 2$. SPT2349-56 clearly stands out as the densest collection of SMGs: although some other protoclusters contain as many SMGs, they extend over much larger areas on the sky, with separations often exceeding 10 arcmin (800 to 1400 cMpc at $z = 4.3$ to $z = 2$). This comparison demonstrates that SPT2349-56 is likely observed during a significantly more advanced stage of cluster formation than other high-redshift protoclusters, a cluster core in the process of assembly rather than an extended structure that may not even collapse to form a cluster by the present day.[12]

Also shown in Fig. 2 is the maximal curve of growth predicted by a theoretical model for submm-luminous protocluster regions at $z \sim 4.5$ (see Methods for details). Except for SPT2349-56 and the recent Herschel discovery SMM J004224,[24] the comparison high-z protoclusters exhibit $S_{870\,\mu\mathrm{m}}$ curves of growth fairly consistent with the model expectations. The model prediction for the region spanned by SPT2349-56 is $\sim 10\%$ of the observed total flux density of the 14 ALMA sources. The under-prediction is more severe if we consider the extended LABOCA source: only $\sim 5\%$ of the observed flux density is recovered. This discrepancy may suggest that environmental effects (such as enhanced galaxy interactions or gas accretion in high-density environments) that are not included in the theoretical model employed are responsible for the extremely high SFR density exhibited by SPT2349-56. An alternative theoretical approach, 'zoom' hydrodynamical simulations of protoclusters,[25] can potentially capture such environmental effects, but to date, such simulations have been unable to reproduce the extremely high SFR inferred for SPT2349-56: of the 24 protocluster simulations presented by these authors, the maximum total SFR attained was ~ 1700 $\mathrm{M}_{\odot}\,\mathrm{yr}^{-1}$, an order of magnitude less than that of SPT2349-56. However, the volume of the N-body simulation from which the 24 halos were selected was 1 h^{-3} cGpc^3, which may be too small to contain an object as rare as SPT2349-56. Nevertheless, the existence of SPT2349-56, which contains an unprecedented concentration of rapidly star-forming SMGs when the Universe was only 1.4 Gyr old, poses a formidable challenge to theoretical models seeking to explain the origin and evolution of galaxy (proto)clusters.

SPT2349-56 may represent a significantly more advanced stage of cluster formation than the typical $z > 4$ protoclusters identified to date, as outlined above. Since the cores of present-day galaxy clusters are characterized by massive elliptical galaxies with old-to-intermediate-age stellar populations[26] and SMGs are thought to be the high-redshift progenitors of present-day ellipticals,[23] it is likely that the 14 SMGs located at the same redshift within a region < 130 kpc in diameter will soon merge to form a massive elliptical galaxy at the core of a lower-redshift galaxy cluster. This can be quantified by considering the total energy per unit mass of the system $E = 1/2v^2 + \Phi$ (km s^{-1})^2. The total energy is negative for the 14 sources, assuming the individual halo masses are as little as $\geq 2\times$ the masses implied by their central line widths, a condition that is easily met for any local galaxies.[27] Theoretical studies have shown that at $z > 4$, the progenitors of galaxy clusters should span > 5 comoving Mpc (cMpc),[12,28] corresponding to an angular scale of as much as a degree; we are thus possibly observing only a small part of a much larger structure. For SPT2349-56, it is unknown whether the overdensity extends over such a large scale, as more detailed observations are required to characterize the field surrounding SPT2349-56. We have demonstrated that the extended LABOCA-detected complex has submm colours similar to the core region identified by our ALMA observations and is thus likely all at $z \sim 4.3$. We have also identified five additional bright SPIRE sources in the surrounding $\sim 800 \times 800$ cMpc field with similar red colours lying several arcmin from the core structure (see Methods). These are candidates for additional protocluster members located in an extended, collapsing structure, similar to the comparison SMG overdensities shown in Fig. 2. If all these sources are confirmed to lie at $z = 4.31$, this would approximately double the far-IR luminosity of the cluster, making it by far the most active system known in the Universe. Since SPT2349-56 was selected from a blind mm survey of 2500 deg^2 (approximately 1/16th of the sky), it is unlikely there are more than approximately 16 such structures across the entire sky. A full analysis of other unlensed sources from the SPT survey to identify possible systems similar to SPT2349-56 will place stronger constraints on early structure formation in the Universe.

References

[1] Wang, T. *et al.* Discovery of a galaxy cluster with a violently starbursting core at $z = 2.506$. *The Astrophysical Journal* **828**, 56 (2016).

[2] Mantz, A. B. *et al.* The XXL Survey: XVII. X-ray and Sunyaev-Zel'dovich Properties of the Redshift 2.0 Galaxy Cluster XLSSC 122. *ArXiv e-prints* (2017). `1703.08221`.

[3] Stanford, S. A. *et al.* IDCS J1426.5+3508: Discovery of a Massive, Infrared-Selected Galaxy Cluster at $z = 1.75$. *The Astrophysical Journal* **753**, 164 (2012).

[4] Springel, V. *et al.* Simulating the joint evolution of quasars, galaxies and their large-scale distribution. *Nature* **435**, 629–636 (2005).

[5] Overzier, R. A. *et al.* ΛCDM predictions for galaxy protoclusters - I. The relation between galaxies, protoclusters and quasars at. *Monthly Notices of the Royal Astronomical Society* **394**, 577–594 (2009).

[6] Chiang, Y.-K., Overzier, R. A., Gebhardt, K. & Henriques, B. Galaxy Protoclusters as Drivers of Cosmic Star Formation History in the First 2 Gyr. *The Astrophysical Journal Letters* **844**, L23 (2017).

[7] Miley, G. & De Breuck, C. Distant radio galaxies and their environments. *Astronomy and Astrophysics Review* **15**, 67–144 (2008).

[8] Casey, C. M. *et al.* A massive, distant proto-cluster at $z = 2.47$ caught in a phase of rapid formation? *The Astrophysical Journal Letters* **808** (2015).

[9] Chapman, S. C. *et al.* Do Submillimeter Galaxies Really Trace the Most Massive Dark-Matter Halos? Discovery of a High-z Cluster in a Highly Active Phase of Evolution. *The Astrophysical Journal* **691**, 560–568 (2009).

[10] Tamura, Y. *et al.* Spatial correlation between submillimetre and Lyman-α galaxies in the SSA22 protocluster. *Nature* **459**, 61 (2009).

[11] Ma, J. *et al.* Stellar Masses and Star Formation Rates of Lensed, Dusty, Star-forming Galaxies from the SPT Survey. *The Astrophysical Journal* **812**, 88 (2015).

[12] Chiang, Y.-K., Overzier, R. & Gebhardt, K. Ancient Light from Young Cosmic Cities: Physical and Observational Signatures of Galaxy Proto-Clusters. *The Astrophysical Journal* **779** (2013).

[13] Vieira, J. D. *et al.* Extragalactic Millimeter-wave Sources in the South Pole Telescope Survey Data: Source Counts, Catalog, and Statistics for an 87 Square-Degree Field. *The Astrophysical Journal* **719**, 763–783 (2010).

[14] Mocanu, L. M. *et al.* Extragalactic millimeter-wave point source catalog, number counts and statistics from 771 square degrees of the SPT-SZ Survey. *The Astrophysical Journal* **779** (2013).

[15] Vieira, J. D. *et al.* Dusty starburst galaxies in the early Universe as revealed by gravitational lensing. *Nature* **495**, 344–347 (2013).

[16] Spilker, J. *et al.* ALMA Imaging and Gravitational Lens Models of South Pole Telescope-Selected Dusty, Star-Forming Galaxies at High Redshifts. *The Astrophysical Journal* **826**, 112 (2016).

[17] Strandet, M. L. *et al.* The redshift distribution of dusty star forming galaxies from the SPT survey. *The Astrophysical Journal* **822**, 80 (2016).

[18] Liang, L. *et al.* The growth and enrichment of intragroup gas. *Monthly Notices of the Royal Astronomical Society* **456**, 4266–4290 (2016).

[19] Beers, T. C. *et al.* Measures of location and scale for velocities in clusters of galaxies - A robust approach. *The Astronomical Journal* **100**, 32 (1990).

[20] Evrard, A. E. *et al.* Virial Scaling of Massive Dark Matter Halos: Why Clusters Prefer a High Normalization Cosmology. *The Astrophysical Journal* **672**, 122–137 (2008).

[21] Cole, S., Helly, J., Frenk, C. S. & Parkinson, H. The statistical properties of Lambda cold dark matter halo formation. *Monthly Notices of the Royal Astronomical Society* **383**, 546–556 (2008).

[22] Ono, Y., Ouchi, M., Kurono, Y. & Momose, R. Faint Submillimeter Galaxies Revealed by Multifield Deep ALMA Observation: Number Counts, Spatial Clustering, and a Dark Submillimeter Line Emitter. *The Astrophysical Journal* **795**, 5 (2014).

[23] Simpson, J. M. *et al.* An ALMA Survey of Submillimeter Galaxies in the Extended Chandra Deep Field South: The Redshift Distribution and Evolution of Submillimeter Galaxies. *The Astrophysical Journal* **788**, 125 (2014).

[24] Oteo, I. *et al.* An extreme proto-cluster of luminous dusty starbursts in the early Universe. *ArXiv e-prints* (2017). 1709.02809.

[25] Granato, G. L. *et al.* The early phases of galaxy clusters formation in IR: Coupling hydrodynamical simulations with GRASIL-3D. *Monthly Notices of the Royal Astronomical Society* **450**, 1320–1332 (2015).

[26] Renzini, A. Stellar Population Diagnostics of Elliptical Galaxy Formation. *Annual Review of Astronomy and Astrophysics* **44**, 141–192 (2006).

[27] Ibata, R. A. *et al.* A vast, thin plane of corotating dwarf galaxies orbiting the Andromeda galaxy. *Nature* **493**, 62–65 (2013).

[28] Oñorbe, J. *et al.* How to zoom: Bias, contamination and lagrange volumes in multimass cosmological simulations. *Monthly Notices of the Royal Astronomical Society* **437**, 1894–1908 (2013).

[29] Weiß, A. *et al.* ALMA Redshifts of Millimeter-Selected Galaxies From the SPT Survey: The Redshift Distribution of Dusty Star-Forming Galaxies. *The Astrophysical Journal* **767**, 88 (2013).

[30] Behroozi, P. S., Wechsler, R. H. & Conroy, C. The Average Star Formation Histories of Galaxies in Dark Matter Halos From $z = 0-8$. *The Astrophysical Journal* **770**, 57 (2013).

Acknowledgments
This paper makes use of the following ALMA data: ADS/JAO.ALMA#2016.0.00236.T and ADS/JAO.ALMA#2015.1.01543.T. ALMA is a partnership of ESO (representing its member states), NSF (USA) and NINS (Japan), together with NRC (Canada) and NSC and ASIAA (Taiwan), in cooperation with the Republic of Chile. The Joint ALMA Observatory is operated by ESO, AUI/NRAO and NAOJ. This work is also based in part on observations made with the Spitzer Space Telescope, which is operated by the Jet Propulsion Laboratory, California Institute of Technology under a contract with NASA. The SPT is supported by the National Science Foundation through grant PLR-1248097, with partial support through PHY-1125897, the Kavli Foundation and the Gordon and Betty Moore Foundation grant GBMF 947. This publication is based on data acquired with the Atacama Pathfinder Experiment (APEX) under programme IDs E-299.A-5045A-2017 and ID M-091.F-0031-2013. APEX is a collaboration between the Max-Planck-Institut fur Radioastronomie, the European Southern Observatory, and the Onsala Space Observatory. Supporting observations were obtained at the Gemini Observatory, which is operated by the Association of Universities for Research in Astronomy, Inc., under a cooperative agreement with the NSF on behalf of the Gemini partnership: the National Science Foundation (United States), the National Research Council (Canada), CONICYT (Chile), Ministerio de Ciencia, Tecnologa e Innovacion Productiva (Argentina), and Ministerio da Ciencia, Tecnologia e Inovacao (Brazil). The Australia Telescope Compact Array (ATCA) is part of the Australia Telescope National Facility which is funded by the Australian Government for operation as a National Facility managed by CSIRO. D.P.M., J.S.S., J.D.V., K.C.L., and S.J. acknowledge support from the U.S. National Science Foundation under grant AST-1312950. S.C.C., T.B.M., and A.B. acknowledge support from NSERC. S.C.C. and T.B.M. acknowledge CFI and the Killam trust. M.A. acknowledges partial support from FONDECYT through grant 114009 The Flatiron Institute is supported by the Simons Foundation. J.D.V. acknowledges support from an A.P. Sloan Foundation Fellowship.

Author Contributions T.B.M. led the data analysis, and assembled the paper. S.C.C. designed the study, proposed the ALMA observations, reimaged the data, and analyzed the data products. C.C.H. developed the theoretical model and advised on the literature comparison. M.A. led the ATCA follow-up and the blind emission line studies. A.W. procured and analyzed the deep LABOCA imaging. M.B. provided the cluster mass and evolution context and discussion. J.S. reimaged the calibrated data. K.A.P. preform the SED fitting. T.B.M, M.A., K.A.P. and A.W. made the figures. S.C.C., T.B.M., M.A., C.C.H., D.M., J.D.V., and A.W. wrote the manuscript. All authors discussed the results and provided comments on the paper. The authors are ordered alphabetically after A.W.

Author Information The authors declare no competing financial interests. Correspondence and requests for materials should be addressed to T.B.M. at tim.miller@yale.edu

Methods

1 Observations

1.1 SPT, LABOCA, and Herschel discovery and ALMA follow-up

The South Pole Telescope[31] (SPT) possesses a unique combination of sensitivity, selection wavelengths (3, 2, and 1.4 mm), and beam size that potentially make it ideal for finding the active core regions of galaxy clusters forming at the earliest epochs. Finding very distant ($z > 4$), gravitationally lensed millimetre sources in the SPT survey is relatively straightforward, where the contrast to such distant bright sources is high relative to the weak (generally undetected) galactic foregrounds (Extended Data Figure 1). However searching for the rare SMGs in the SPT 2500 deg^2 survey that are unlensed, and therefore candidates for active groups and protoclusters like SPT2349-56, involves sifting through the many gravitationally lensed sources, and typically involves multi-stage follow-up efforts using various facilities: a single dish mapping instrument like APEX-LABOCA to better localize the emission within the $\sim 1'$ SPT beam, deep optical imaging to search for bright lensing galaxies, and high resolution ALMA mapping. The spatially extended sources in SPT2349-56 found with LABOCA span more than an arc min.. With deep upcoming surveys using the next generation SPT-3G receiver, this 'extended-beam' thermal source structure may present a unique signature of many early forming protoclusters, affording the first complete census in the early epochs of structure formation.

A shallow, wide field SPIRE image over a 100 deg^2 subregion of SPT-SZ[32] reveals the red colours of SPT2349-56, and that SPT2349-56 appears to reside in something of a void in the $z \sim 1$ foreground that dominates the SPIRE galaxy population. However the high redshift of SPT2349-56 means that it is not significantly brighter than many other SPIRE sources in this field, and aside from its colours, SPT2349-56 does not stand out substantially from the field despite its extreme properties. SPT2349-56 is not detected in the all sky Planck survey,[33] the lower sensitivity of Planck compared with SPT being exacerbated by beam dilution in the $3'$ beam.

Obtaining the redshift for SPT2349-56 was beyond the scope of the original SPT-SMG redshift survey, due to the faintness of the unlensed components relative to the typical bright, gravitationally lensed SMGs found in the bulk of the SPT-SMG sample. In ALMA Cy 1, SPT2349-56 was included in the 3-mm spectral scan redshift survey,[15,29] but no lines were detected in the short $\sim$ 1min integrations with 16 ALMA antennae. In Cy 3, a deeper follow-up 3-mm spectral scan was able to tentatively identify two CO lines and a double source structure with a likely redshift $z = 4.30$, confirmed by APEX/FLASH C+ detection.[17]

1.1.1 APEX - LABOCA

We obtained 870-μm imaging of SPT2349-56 using LABOCA on the APEX telescope. A shallow image with 1.6hr integration time was observed on 27 Sep 2010 reaching ~ 5 mJy/beam rms. In August 2017 we obtained a deeper image (18.8h integration time, Project ID: E-299.A-5045A-2017) reaching a reaching a minimum noise level of 1.3 mJy/beam and < 2.0 and < 1.5 mJy/beam rms for 75.3 and 32.4 sq arcmin, respectively (shown in Figure 1 & Extended Data Figure 2). All observations were carried out using standard raster-spiral observations[34] under good weather conditions (PWV of 0.6 mm and 0.8 mm for the 2010 and 2017 observing campaigns, respectively). Calibration was achieved through observations of Uranus, Neptune and secondary calibrators and was found to be accurate within 8.5% rms. The atmospheric attenuation was determined via skydips every 2hr as well as from independent data from the APEX radiometer which measures the line of sight water vapor column every minute. The data was reduced and imaged using the BoA reduction package.[35] LABOCA's central frequency and beam size are 345 GHz and 19.2$''$, resolving the SPT 1.4-mm elongated source into two bright LABOCA sources.

Both LABOCA observations yield consistent calibration results with peak intensity at 21$''$ resolution of 50 mJy/beam for the brighter, southern component (RA 23:49:42.70, DEC -56:38:23.4). In addition the LABOCA map reveals a second source to the north at RA: 23:49:42.86, DEC: -56:37:31.02 with a peak flux density at 21$''$ resolution of 17 mJy/beam. Both sources are clearly extended even at LABOCA's relatively coarse spatial resolution with deconvolved source size of 18$''\times$12$''$ and 32$''\times$5$''$ for the sourthern and northern source, respectively. These components are connected by a faint bridge emission. The total 870-μm flux density of the SPT2349-56 system is 110.0$\pm$9.5 mJy, of which $\sim$77 mJy are associated with the southern component, $\sim$25 mJy with the northern component, and $\sim$7 mJy with the connection between the components (using the sub apertures shown in Extended Data Figure 2). One additional submm source is detected at $> 5\sigma$ in the LABOCA image to the east of the primary source, but having blue colours inconsistent with $z \sim 4$, and not likely being a member of the extended protocluster.

1.2 ALMA

Observations using ALMA Band-3 targeted the CO(4-3) line in SPT2349-56 centred in the lowest frequency of the spectral windows adopted (86-88 GHz), taken under a Cycle 3 program 2015.1.01543.T (PI: K. Lacaille). Data was taken on June 24th, 2016 with a 47 min integration time. The array used 36 antennas with baselines ranging from 15 to 704 m, and provided a naturally weighted synthesized beam size of $\sim 1''$. Pallas and J2343-5626 were used to calibrate the flux and phase respectively. Data was processed using the standard ALMA pipeline using natural beam weighting.

ALMA Band-7 imaging (276 GHz) were obtained under a Cycle 4 program (2016.0.00236.T; PI: S. Chapman) targeting the peak of the brightest LABOCA source. Observations were obtained on December 14th, 2016 in a 40-2 array configuration with baseline lengths of 15-459 m, giving a naturally weighted synthesized beam size of $\sim 1''$. There were 40 antennas available, with total on source integration time of 22 minutes. Ceres and J2357-5311 were used as flux and phase calibrators respectively. The [CII] line ($\nu_{rest} = 1900.5\,$GHz) was observed at as part of the same ALMA project on March 23rd, 2017, tuning in Band 7 to the redshifted line at $\nu_{ons} = 358.3\,$GHz in the upper sideband covering 356 to 360 GHz. These observations used the 40-2 array configuration with baselines of 16-459 m, giving a naturally weighted synthesized beam size of $\sim 0.5''$. An on-source integration time of 14 min was obtained, and J2357-5311 was used as both the flux and phase calibrator. The data were re-processed using CASA and the standard ALMA-supplied calibration using natural beam weighting to maximize sensitivity.

One dimensional spectra are extracted from the centroid of the line emission for each source and binned into 75 km s^{-1} channels. Spectra are presented in Figure 1, and are smoothed using a Gaussian filter with FWHM = 100 km s^{-1} for presentation. A Gaussian line profile is fit using a least-squares method, providing errors to the velocity offsets from $z = 4.300$ in Table 1 and line widths in Extended Data Table 2. The continuum level is left as a free parameter in the fitting function which is then subtracted to derive line fluxes.

1.2.1 Blind search for [CII]

We performed a blind search for [CII] line emission in the ALMA band 7 data cube toward SPT2349-56. For this, we follow the procedure used to detect line emitters in the ASPECS survey.[36] We use a data cube channelized at 100 km/s, without primary beam correction and continuum subtraction.

We used the Astronomical Image Processing System (AIPS) task SERCH. This task convolves the data cube along the frequency axis with a Gaussian kernel defined by different input linewidths, subtracts surrounding continuum, and reports all channels and pixels that have a signal-to-noise ratio (SNR) over a specified limit. The SNR is defined as the maximum significance level achieved after convolving over the Gaussian kernels. We used a set of different Gaussian kernels, from 200 to 600 km/s and searched for all line peaks with SNR>4.0.

Once all peaks were identified, we used the IDL routine CLUMPFIND[37] to isolate individual candidates. A full list of 68 positive line peaks with SNR>4.0 were thus obtained. We quantified the reliability of our line search based on the number of negative peaks in our ALMA cube, using the same line procedure. We find 43 negative peaks with SNR<5.8. This means that all positive line candidates with SNR>6.0 are likely real (100% purity). Out of the 14 [CII] line candidates detected, all have SNR>6.3 and 13 are associated with continuum detections in the ALMA data.

1.3 ATCA CO(2-1)

1.3.1 Observations

We used the Australia Telescope Compact Array (ATCA) in its H168 hybrid array configuration to observe the CO(2-1) emission line ($\nu_{\rm rest} = 230.5380\,$GHz) toward SPT2349-56 (with a primary beam size of 53″). The observations were performed as part of project ID C2818 during 2016 October 2,3 and 11 under good weather conditions (atmospheric seeing values 90-400 m) with five working antennas.

We used the ATCA 7-mm receivers, with the Compact Array Broadband Backend configured in the wide bandwidth mode.[38] This leads to a total bandwidth of 2 GHz per correlator window and a spectral resolution of 1 MHz per channel (6.9 km/s per channel). The spectral windows were centred at observing frequencies of 43.5 and 45.0 GHz, and aimed at observing the CO line and continuum emission, respectively.

Gain and pointing calibration were performed every 10 min and 1 h, respectively.The bright sources 1921-293, 1934-638 and 2355-534 were used as bandpass, flux and gain calibrators, respectively. We expect the flux calibration to be accurate to within 15 per cent, based on the comparison of the Uranus and 1934-638 fluxes. The software package MIRIAD[39] and the Common Astronomy Software Applications (CASA[40]) were used for editing, calibration and imaging.

The calibrated visibilities were inverted using the CASA task CLEAN using natural weighting. No cleaning was applied given the relatively low significance of the CO line detection in individual channels. The final data cube, averaged along the spectral axis, yields an rms of 0.23 mJy beam^{-1} per 100 km/s channel with a synthesized beam size of 5.6″×4.5″ (PA=70.4 deg) at 43.5 GHz.

1.3.2 Results

One source formally detected at the centre, which corresponds to CII/continuum sources B+C+G. This central CO source (C) is unresolved at the resolution of the ATCA observations. Other two sources are marginally detected to the East (E) and North (N) of the central source, coinciding with the location of CII/continuum sources D+E and A+K, respectively. We extracted spectra at these locations and obtained integrated line intensities, by fitting Gaussian profiles to the identified line emission.

We compute CO luminosities using the integrated line intensities and compute gas masses by assuming a ULIRG X_{CO} factor of 0.8 ($M_\odot$ (K km/s pc^2)$^{-1}$) and that the CO gas is in local thermodynamic equilibrium thus $L'_{(CO2-1)} \sim L'_{(CO1-0)}$.[41] The results of the CO line observations are summarized in Extended Data Table 2. Collapsing the line-free spectral window along the spectral axis over the 2-GHz bandwidth, leads to a non-detection of the continuum emission down to 80 μJy/beam (3σ).

These results confirm the finding from CO(4-3) line that that the main reservoir (72%) of molecular gas resides in the B+C+G system, with a smaller fraction hosted at the East and North locations.

1.4 Spitzer imaging

This field was twice observed at 3.6 and 4.5 μm with the Infrared Array Camera (IRAC[42]) on board the *Spitzer Space Telescope*.[43] It was first observed in 2009 August as part of a large program to obtain follow-up imaging of a large sample of SPT-selected SMGs sources (PID 60194, PI Vieira). The observing scheme used for PID 60194 was to obtain 36 dithered 100 sec integrations at 3.6 μm and, separately, a much shallower 12×30 sec integration at 4.5 μm. Later, in Cycle 8, the field was covered serendipitously as part of the *Spitzer*-SPT Deep Field survey (PID 80032, PI Stanford; Ashby et al. 2013). PID 80032 surveyed 92 deg^2 uniformly in both IRAC passbands to a depth of 4×30 sec. Using established techniques, we combined all exposures covering the SPT target from PID 60194 and 80032 at 3.6 and 4.6 μm to obtain the best possible S/N in our final mosaics, which were pixellated to 0.5″. Nine of the 14 sources identified by ALMA are detected in the IRAC bands at $> 3\sigma$ in at least one of the 3.6 or 4.5 μm channels, as shown in Extended Data Figure 4.

1.5 Analysis of the surrounding field with SPIRE and LABOCA imaging

In Extended Data Figure 5, our deep SPIRE RGB image is shown with LABOCA contours overlaid. A source sample is culled from the 250 μm-selected catalog (135 sources with SNR(250 μm)>3 in an area of 52 arcmin^2), where the source peaks are best defined. To account for the large beam size difference with SPIRE (ranging from 36″ at 500 μm to 18″ at 250 μm), we employed a deblending code, using the 250 μm positions as spatial priors, which provides the standard parameters as well as the covariance matrices highlighting the degeneracies (almost none at 250 μm, but significant at 500 μm). The code, FASTPHOT,[44] takes into account these degeneracies to estimate the flux measurement errors.

Colour-colour (CC) and colour-flux (CF) diagrams are shown in Extended Data Figure 5. The CC diagram shows a 250 μm-selected sample with SNR(250 μm)>3 and is dominated by the $z \sim 1$ cosmic infrared background (blue, green colours) in the *foreground* of SPT2349-56. The CF diagram shows an additional SNR(500 μm)>3 cut to highlight just the well detected 500 μm source sub-sample. These diagrams highlight the extreme and red properties of SPT2349-56, but make clear that one of the three 250 μm-peaks within the SPT2349-56 LABOCA structure is very likely a foreground galaxy (green symbol highlighted in the figure shows very blue colours). Nevertheless, a full ALMA mapping of the structure is warranted given the uncertainties involved in the SPIRE deconvolution procedure.

Five red sources consistent with $z \sim 4$ ($S_{500\,\mu\mathrm{m}} > S_{350\,\mu\mathrm{m}} > S_{250\,\mu\mathrm{m}}$) are found in the surrounding $\sim 10' \times 10'$ field and are candidates for additional protocluster members in an extended, collapsing structure. If all these sources were bona fide $z = 4.3$ sources, this would significantly increase the total 870-μm flux density (and thus the far-IR luminosity) of the cluster beyond the 110 mJy found in the central structure, making it by far the most active system known in the Universe (see Figure 2).The deep LABOCA map marginally detects the closest of the five red SPIRE sources at $\sim 3\sigma$, consistent with expectations given the SPIRE flux densities.

Full analysis of these surrounding SMGs will require additional follow-up efforts.

2 Properties, Comparisons, Simulations

2.1 Derivation of physical properties

We briefly describe our procedures for calculating various physical quantities from observables below. To derive SFR, we measure 870-μm flux density directly in the lower sideband (line-free bands) of our ALMA Band-7 observations from Cycle 4, finding consistent measurements with those found in previous shallower observations.[16] We adopt an SFR-to-$S_{870\,\mu\mathrm{m}}$ ratio of 150 $\pm$ 50 $\mathrm{M}_\odot\,\mathrm{yr}^{-1}$/mJy, which is typical for SMGs.[45] The uncertainty in this ratio owes to variations in the dust temperature distribution amongst the SMG population, which are primarily driven by differences in the ratio of the luminosity absorbed by dust to the total dust mass.[46] This combined with the measurement error dictates the error on the SFR shown in Table 1

Gas mass is calculated from the CO(4-3) line luminosity, which is converted to CO(1-0) luminosity using a ratio between the brightness temperatures of these lines $r_{4,1} = 0.41 \pm 0.07$ found from the average of a sample of unlensed SMGs with multiple CO line transitions detected.[47] We use a conservative conversion factor $\alpha_{CO} = 0.8 \frac{\mathrm{M}_\odot}{\mathrm{K\,km\,s^{-s}\,pc^2}}$ and multiply by 1.36 to account for the addition of helium. When CO(4-3) is not significantly detected, we use our [CII] line luminosity and the average CO(4-3)/[CII] ratio for our detected sample; we denote these sources with asterisks in Table 1.

The dynamical masses of galaxies are estimated using the following relation for a dispersion-dominated system, with $C = 1.56$ for a spherical distribution:

$$\mathrm{M_{dyn}(M_\odot)} = C \times 10^6 \sigma_V^2 R \qquad (1)$$

where σ_v is the line-of-sight velocity dispersion in km s^{-1} calculated from the Gaussian fit to each line profile and R is the radius fit to the 345-GHz continuum of each source. Size for all sources are calculated by a 2D Gaussian fit to each source deconvolved with the naturally weighted synthesized beam (0.5$''$ FWHM), although most are only marginally resolved in the image beyond the beam. For the smallest sources, where the error on the fit is not significant above the beam size, we adopt the 0.5$''$ FWHM beam as an upper limit on the source size. Sizes for the sources are displayed in Extended Data Table 1 We use σ_v from the CO(4-3) profile for all sources except H, K, L, M, and N, where [CII] profile is used because CO(4-3) is not detected.

2.2 Spectral energy distribution of SPT2349-56

The SPT, LABOCA and SPIRE measurements resolve the SPT2349-56 structure to varying degrees, but none can isolate the core region resolved by our current ALMA observations with any confidence. We thus assemble a photometric catalog of the total SPT2349-56 flux density from 250 μm to 3 mm and model the resulting total SED to estimate some global properties of the system. We do not include the SPT 1.4, 2.0, and 3.0 mm points because the source is elongated and flux measurements are difficult with the filtering used to make the map. At IRAC wavelengths in the mid-infrared, we detect 9 SMGs significantly and use these to determine a lower limit on the stellar mass assembled to date in SPT2349-56.

We have used Code Investigating GALaxy Emission (CIGALE)[48,49] for the SED fitting of the combined photometry of the source. The SED modelling assumes a single-component star formation history and solar metallicity.[50] A Chabrier[51] IMF is assumed. The resulting best-fitting SED is shown in Extended Data Figure 7. The IR luminosity (from 8–1100 μm) is $(8.0 \pm 1.0) \times 10^{13}$ $L_\odot$. The stellar mass inferred for this fit is highly uncertain, i.e., $9.5 \times 10^{11} \pm 1.3 \times 10^{12}$ solar masses. The best-fit SED corresponds to a stellar mass of 4.5$\times 10^{11}$ solar masses, which is a lower limit on the stellar mass because not all the sources are detected in the IRAC bands. More optical-NIR photometry is needed to better constrain the total stellar mass of the system

2.3 Protocluster comparison sample

To place SPT2349-56 in context and compare to other systems claimed to be protoclusters, we assemble from the literature various SMG-rich overdensities at $2 < z < 5$. Although a direct comparison of the number counts (number/deg^2) of SMG-overdense systems can be performed, it involves making somewhat arbitrary choices of enclosed areas and redshift boundaries. We have opted in Figure 2 to instead show a curve of growth analysis of the 870-μm flux density. Only galaxies confirmed to be protocluster members via spectroscopic redshifts are considered. The data are drawn from a recent compilation[52] and original references therein.

The GOODS-N overdensity at $z = 1.99$[9,53,55] spans a $\sim 10'$ by $10'$ field in the Hubble Deep Field North containing 9 SMGs in Δz = 0.008. The probably of finding this large of an overdensity being drawn from the field distribution by chance is $< 0.01\%$. Interestingly, only a modest overdensity of Lyman-break galaxies is found in this GOODS-N structure. The COSMOS $z = 2.5$ SMG overdensity[8] is similar to the GOODS-N structure in terms of the numbers and luminosities of the component SMGs, the angular size of the system, and the modest overdensity of LBGs associated with it. The MRC1138 overdensity was originally discovered as an overdensity of Lyα and Hα emitters.[57] Follow-up observations[58,59] revealed the presence of 5 SMGs, in addition to an AGN known as the 'Spiderweb galaxy'. This is a radio-loud AGN that resides in a large Ly-α halo. The SSA22 protocluster was one of the first discovered by observing an overdensity of LBGs.[60] It is an extremely extended structure located at $z = 3.09$, with LAEs spanning greater than 50 comoving Mpc (cMpc).[61] Submm observations of the field have revealed a population of at least eight SMGs[10,53,62,63,65] .

The COSMOS $z = 2.1$ protocluster[66] lacks sufficiently deep 850-μm data to characterize the *Herschel*-SPIRE sources identified in the structure. We estimate 870-μm flux densities by taking their published $L_{\rm IR}$ (integrated over 3–1100 μm) and use the SED of Arp 220 to estimate $S_{870\,\mu{\rm m}}$, finding that $L_{\rm IR} = 2 \times 10^{12}$ $L_\odot$corresponds to $S_{870\,\mu m}$ = 1 mJy at $z \sim 2$. For the SSA22 protocluster, we use the measured 870-μm flux density when available and otherwise estimate it from the 1.1-mm flux using a standard conversion at $z \sim 3$ of $S_{870\,\mu m} = 2\times S_{1.1\,\rm mm}$. To create the curves of growth for Figure 2, the centre of each protocluster is defined by computing the median RA and DEC of all submm sources. We checked that adjusting the centres of the curve of growth tracks randomly by $\sim 1'$ did not boost the curves by more than 10%, demonstrating that the curves of growth for the literature SMG overdensities are insensitive to the adopted centre.

Recently, there have also been detections of SMG overdensities at $z > 4$. The first, GN20, at $z = 4.05$, was discovered through the serendipitous detection of CO(4-3) from two SMGs,[67] with two further SMGs detected subsequently.[68] An excess of B-band dropouts is also observed in this structure, several of which are spectroscopically confirmed to lie at $z \sim 4.05$. HDF850.1 contains a single SMG, a QSO, and 11 spectroscopically confirmed galaxies. The SMG has a confirmed redshift of $z = 5.18$.[69] The *AzTEC-3* overdensity is centred on a single SMG at $z = 5.3$, with 12 spectroscopically confirmed optical galaxies at the same redshift. This is a relatively dense structure, with most of the galaxies residing within a circle $\sim 1'$ in diameter. The most luminous example at $z > 4$, SMM J004224, was recently found from the *Herschel* surveys,[24] with several additional 870μm sources in the field which the authors claim may be related to the central source by their over density (characterized as twice the over density of the blank field counts). In Fig. 2 we place all of their surrounding sources in the comparison, however on average about half of these sources are likely to be in the protocluster.

Overdensities of SMGs and optical galaxies have also been found around high-redshift radio galaxies (HzRGs),[70] continuing to confirm HzRGs as useful beacons of structure forming in the early Universe. However none of these systems come close to the level of overdensity found in SPT2349-56, and furthermore, they suffer from the bias inherent in targeting these sources, namely, that one or more protocluster members have to be radio-luminous.

There have also been discoveries of compact binary HyLIRG systems, the most luminous of which is the $z = 2.4$ source HATLAS J084933,[71] with others approaching this luminosity.[72,73] In each of these systems, the dynamics and SFRs are dominated by two SMGs, but there is no strong evidence of any surrounding protocluster in the form of an excess of galaxies selected optically or in the submm. In one case,[73] there is evidence for a relative void around the structure. These systems may simply be instances of very rare events in fairly typical (but still massive) halos,[74] analogous to hyper-luminous quasars.[75]

Theoretical studies of N-body simulations have shown that the progenitors of $z = 0$ dark matter halos with masses $> 10^{15}$ $M_\odot$ should extend over length-scales of $\gtrsim 5$ cMpc at $z > 2$.[12,28] Since the overdensities listed above are mostly concentrated in small areas, it is difficult to asses their exact evolution or compare them easily to simulated structures. Interpreting a small overdense region at high-redshift as a 'protocluster core' is certainly prone to misinterpretation, and small overdense regions at high redshift can evolve into halos spanning a range of masses at the current epoch.[12] These authors suggest investigating if an overdensity extends to larger scales (> 20 cMpc) to better determine whether it will form an $M \gtrsim 10^{15} M_\odot$cluster. However this is difficult at high redshift because the excess of galaxies will be less pronounced on larger scales, and it is challenging to detect high-redshift, low-luminosity galaxies.

2.4 Simulations

To further place SPT2349-56 in context, we compare with the predictions of a theoretical model for SMG overdensities.[74,76] We employ the MultiDark[77] N-body simulation, which is one of the largest (2.91 Gpc^3) available N-body simulations that still resolves SMG-like halos ($M_{\text{halo}} \gtrsim 10^{12}$ $\text{M}_\odot$). The $z = 4.68$ and $z = 4.1$ snapshots, which are the available snapshots closest in redshift to SPT2349-56, are analyzed. Halo catalogs were created using the Rockstar halo finder,[78] and stellar masses are assigned to dark matter halos using a relation derived based on sub-halo abundance matching relation.[30] To assign SFRs, it is assumed that the distribution of specific SFR (SFR per unit stellar mass, hereafter SSFR) is the sum of two Gaussians, corresponding to quiescently star-forming and starburst galaxies.[79] The median SSFR value is based on the abundance-matching-derived relation,[30] and the starburst fraction and the widths of the Gaussian distributions are set based on observations of massive, high-redshift star-forming galaxies similar to the members of SPT2349-56.[79] M_{d} is estimated from stellar mass using empirical gas fraction and metallicity relations.[80] Once SFR, $M_\star$, and M_{dust} values are assigned to each halo, $S_{870\,\mu\text{m}}$ is calculated using the following fitting function, which was derived based on the results of performing dust radiative transfer on hydrodynamical simulations of both isolated and interacting galaxies:[76,81]

$$S_{870\,\mu\text{m}} = 0.81 \text{ mJy} \left(\frac{\text{SFR}}{100\ \text{M}_\odot\ \text{yr}^{-1}}\right)^{0.43} \left(\frac{M_{\text{d}}}{10^8\ \text{M}_\odot}\right)^{0.54}, \tag{2}$$

where $S_{870\,\mu\text{m}}$ is the 870-μm flux density, SFR is the star formation rate, and M_{d} is the dust mass. Scatter of 0.13 dex is included when applying the relation.

Once $S_{870\,\mu\text{m}}$ has been assigned to each halo, we search the entire simulation volume for the most luminous regions. We begin at each independent halo and calculate the total $S_{870\,\mu\text{m}}$ of all halos within a given radius r of this halo. For each value of r, we record the largest total $S_{870\,\mu\text{m}}$ obtained (across all halos). One hundred Monte Carlo iterations are performed for each snapshot; in each iteration, galaxy properties are re-assigned, drawing from the distributions described above. The shaded region in Figure 2 shows the entire region spanned by the 100 realizations of the maximum $S_{870\,\mu\text{m}}$ vs. area curves. To compare to SPT2349-56 to lower redshift proto-clusters we preform a similar analysis on a snapshot at $z = 2.49$ with 20 Monte Carlo iterations.

Additional References

[31] Carlstrom, J. E. *et al.* The 10 Meter South Pole Telescope. *PASP* **123**, 568 (2011).

[32] Ashby, M. L. N. *et al.* The Spitzer South Pole Telescope Deep Field: Survey Design and Infrared Array Camera Catalogs. *The Astrophysical Journal Supplement Series* **209**, 22 (2013).

[33] Collaboration, P. *et al.* Planck 2013 results. XXII. Constraints on inflation. *Astronomy & Astrophysics* **571**, A22 (2014).

[34] Siringo, G. *et al.* The Large APEX BOlometer CAmera LABOCA. *Astronomy & Astrophysics* **497**, 945–962 (2009).

[35] Weiß, A. *et al.* LABOCA observations of nearby, active galaxies. *Astronomy & Astrophysics* **490**, 77–86 (2008).

[36] Aravena, M. *et al.* The ALMA Spectroscopic Survey in the Hubble Ultra Deep Field: Search for [CII] Line and Dust Emission in $6 < z < 8$ Galaxies. *The Astrophysical Journal* **833**, 71 (2016).

[37] Williams, J. P. *et al.* Clumpfind: Determining Structure in Molecular Clouds. *Astrophysics Source Code Library* ascl:1107.014 (2011).

[38] Wilson, W. E. *et al.* The Australia Telescope Compact Array Broad-band Backend: Description and first results. *Monthly Notices of the Royal Astronomical Society* **416**, 832–856 (2011).

[39] Sault, R. J., Teuben, P. J. & Wright, M. C. H. A retrospective view of Miriad. *Astronomical Data Analysis Software and Systems IV* **77**, 433 (1995).

[40] Mcmullin, J. P., Waters, B., Schiebel, D., Young, W. & Golap, K. CASA Architecture and Applications. In *Astronomical Data Analysis Software and Systems XVI*, vol. 376, 127 (2007).

[41] Solomon, P. M. *et al.* The Molecular Interstellar Medium in Ultraluminous Infrared Galaxies. *The Astrophysical Journal* **478**, 144–161 (1997).

[42] Fazio, G. G. *et al.* The Infrared Array Camera (IRAC) for the Spitzer Space Telescope. *The Astrophysical Journal Supplement Series* **154**, 10–17 (2004).

[43] Werner, M. W. *et al.* The Spitzer Space Telescope Mission. *The Astrophysical Journal Supplement Series* **154**, 1–9 (2004).

[44] Béthermin, M., Dole, H., Cousin, M. & Bavouzet, N. Submillimeter Number Counts at 250, 350 and 500 microns in BLAST data. *Astronomy and Astrophysics* **516**, 13 (2010).

[45] Barger, A. J. *et al.* Is There a Maximum Star Formation Rate in High-Redshift Galaxies? *The Astrophysical Journal* **784** (2014).

[46] Safarzadeh, M., Hayward, C. C., Ferguson, H. C. & Somerville, R. S. What Shapes the Far-infrared Spectral Energy Distributions of Galaxies? *The Astrophysical Journal* **818**, 62 (2016).

[47] Bothwell, M. S. *et al.* A survey of molecular gas in luminous sub-millimetre galaxies. *Monthly Notices of the Royal Astronomical Society* **429**, 3047–3067 (2013).

[48] Burgarella, D. *et al.* Star formation and dust attenuation properties in galaxies from a statistical ultraviolet-to-far-infrared analysis. *Monthly Notices of the Royal Astronomical Society* **360**, 1413–1425 (2005).

[49] Noll, S. *et al.* Analysis of galaxy spectral energy distributions from far-UV to far-IR with CIGALE: studying a SINGS test sample. *Astronomy and Astrophysics* **507**, 1793–1813 (2009).

[50] Bruzual, G. & Charlot, S. Stellar population synthesis at the resolution of 2003. *Monthly Notices of the Royal Astronomical Society* **344**, 1000–1028 (2003).

[51] Chabrier, G. The Galactic Disk Mass Function: Reconciliation of the Hubble Space Telescope and Nearby Determinations. *The Astrophysical Journal* **586**, L133–L136 (2003).

[52] Casey, C. M. The Ubiquity of Coeval Starbursts in Massive Galaxy Cluster Progenitors. *The Astrophysical Journal* **824**, 36 (2016).

[53] Chapman, S. C., Blain, A. W., Smail, I. & Ivison, R. J. A Redshift Survey of the Submillimeter Galaxy Population. *The Astrophysical Journal* **622**, 772–796 (2005).

[54] Chapman, S. C. *et al.* Do Submillimeter Galaxies Really Trace the Most Massive Dark-Matter Halos? Discovery of a High-z Cluster in a Highly Active Phase of Evolution. *The Astrophysical Journal* **691**, 560–568 (2009).

[55] Blain, A. W., Chapman, S. C., Smail, I. & Ivison, R. Clustering of Submillimeterselected Galaxies. *The Astrophysical Journal* **611**, 725–731 (2004).

[56] Casey, C. M. *et al.* A massive, distant proto-cluster at $z = 2.47$ caught in a phase of rapid formation? *The Astrophysical Journal Letters* **808** (2015).

[57] Kurk, J. D. *et al.* A Search for clusters at high redshift. I. Candidate Lyalpha emitters near 1138-262 at $z = 2.2$. *Astronomy and Astrophysics* **358**, L1–L4 (2000).

[58] Kuiper, E. *et al.* A SINFONI view of flies in the Spiderweb: A galaxy cluster in the making. *Monthly Notices of the Royal Astronomical Society* **415**, 2245–2256 (2011).

[59] Dannerbauer, H. *et al.* An excess of dusty starbursts related to the Spiderweb galaxy. *Astronomy & Astrophysics* **570** (2014).

[60] Steidel, C. *et al.* A Large Structure of Galaxies At Redshift $z \sim 3$ and its Cosmological Implications. *The Astrophysical Journal* **492**, 428–438 (1997).

[61] Hayashino, T. *et al.* Large-Scale Structure of Emission-Line Galaxies at $z = 3.1$. *The Astronomical Journal* **128**, 2073–2079 (2004).

[62] Chapman, S. C. *et al.* Submillimeter Imaging of a Protocluster Region at $z = 3.09$. *The Astrophysical Journal* **548**, L17–L21 (2001).

[63] Geach, J. E. *et al.* A submillimetre survey of Lyman α haloes in the SA 22 protocluster at $z = 3.1$. *Monthly Notices of the Royal Astronomical Society* **363**, 1398–1408 (2005).

[64] Tamura, Y. *et al.* Spatial correlation between submillimetre and Lyman-α galaxies in the SSA22 protocluster. *Nature* **459**, 61 (2009).

[65] Umehata, H. *et al.* ALMA Deep Field in SSA22: A concentration of dusty starbursts in a $z = 3.09$ protocluster core. *The Astrophysical Journal Letters* **815** (2015).

[66] Hung, C.-L. *et al.* Large scale structure around a $z = 2.1$ cluster. *The Astrophysical Journal* **826** (2016).

[67] Daddi, E. *et al.* Two Bright Submillimeter Galaxies in a $z = 4.05$ Protocluster in GOODS-North, and Accurate Radio-Infrared Photometric Redshifts. *The Astrophysical Journal* **694**, 1517–1538 (2009).

[68] Daddi, E. *et al.* A CO Emission Line From the Optical and Near-IR Undetected Submillimter Galaxy GN10. *The Astrophysical Journal* **695**, L176–L180 (2009).

[69] Walter, F. *et al.* The intense starburst HDF 850.1 in a galaxy overdensity at $z \sim 5.2$ in the Hubble Deep Field. *Nature* **486**, 233–236 (2012).

[70] Noirot, G. *et al.* HST Grism Confirmation of Two z˜2 Structures From the Clusters Around Radio-Loud AGN (CARLA) Survey. *The Astrophysical Journal* **830**, 90 (2016).

[71] Ivison, R. J. *et al.* Herschel-ATLAS: a binary HyLIRG pinpointing a cluster of starbursting proto-ellipticals. *The Astrophysical Journal* **772** (2013).

[72] Fu, H. *et al.* The rapid assembly of an elliptical galaxy of 400 billion solar masses at a redshift of 2.3. *Nature* **498**, 338–341 (2013).

[73] Chapman, S. C. *et al.* A millimetre-wave redshift search for the unlensed HyLIRG, HS1700.850.1. *Monthly Notices of the Royal Astronomical Society* **453**, 951–959 (2015).

[74] Miller, T. B., Hayward, C. C., Chapman, S. C. & Behroozi, P. S. The bias of the submillimetre galaxy population: SMGs are poor tracers of the most-massive structures in the $z \sim 2$ Universe. *Monthly Notices of the Royal Astronomical Society* **452**, 878–883 (2015).

[75] Trainor, R. F. & Steidel, C. C. The Halo Masses and Galaxy Environments of Hyperluminous QSO's at $z \sim 2.7$ in the Keck Baryonic Structure Survey. *The Astrophysical Journal* **752**, 39 (2012).

[76] Hayward, C. C. *et al.* Spatially unassociated galaxies contribute significantly to the blended submillimetre galaxy population: predictions for follow-up observations of ALMA sources. *Monthly Notices of the Royal Astronomical Society* **434**, 2572–2581 (2013).

[77] Prada, F., Klypin, A. A., Cuesta, A. J., Betancort-Rijo, J. E. & Primack, J. Halo concentrations in the standard Λ cold dark matter cosmology. *Monthly Notices of the Royal Astronomical Society* **423**, 3018–3030 (2012).

[78] Behroozi, P. S., Wechsler, R. H. & Wu, H.-Y. The Rockstar Phase-Space Temporal Halo Finder and the Velocity Offsets of Cluster Cores. *The Astrophysical Journal* **762** (2011).

[79] Sargent, M. T. *et al.* The Contribution of Starbursts and Normal Galaxies to Infrared Luminosity Functions at $z < 2$. *The Astrophysical Journal* **747**, L31 (2012).

[80] Hayward, C. C. *et al.* Submillimetre galaxies in a hierarchical universe: Number counts, redshift distribution and implications for the IMF. *Monthly Notices of the Royal Astronomical Society* **428**, 2529–2547 (2013).

[81] Hayward, C. C. *et al.* What Does a Submillimeter Galaxy Selection Actually Select? The Dependence of Submillimeter Flux Density on Star Formation Rate and Dust Mass. *The Astrophysical Journal* **743**, 159 (2011).

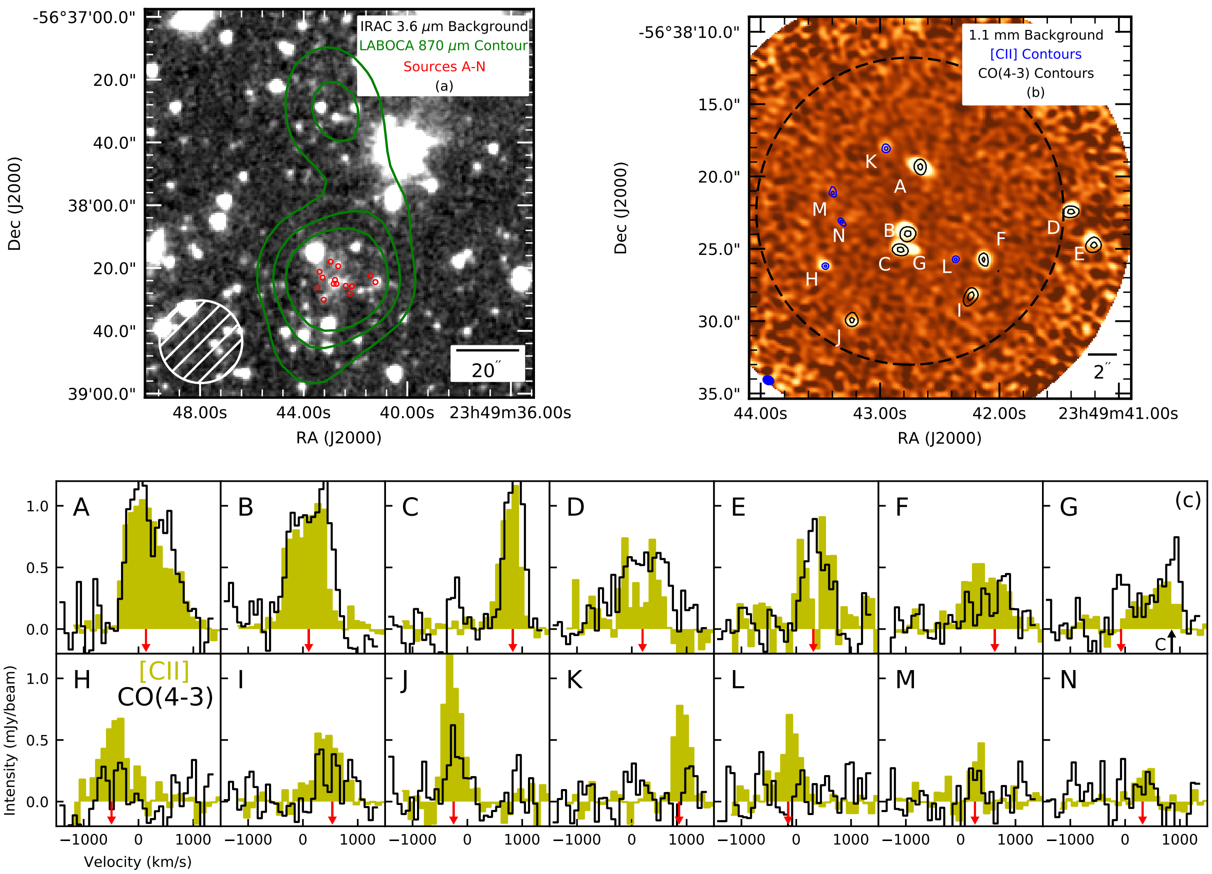

Figure 1: The SPT2349-56 field and spectra of the constituent galaxies. (a) The LABOCA 870-μm contours of SPT2349-56 overlaid on the IRAC 3.6-μm image; the 26″ beam at 870 μm is shown. Contours represent SNR = 3,7 and 9. The small circles show the locations of the 14 protocluster sources. (b) ALMA band 7 imaging (276 GHz, 1.1 mm) displaying the 14 confirmed protocluster sources, labeled A-N. Black (blue) contours denote the points 38% and 50% of the peak flux for each source from the CO(4-3) ([CII]). The dashed black line shows where the primary beam is 50% the maximum. The filled blue ellipse shows the 0.4″ naturally weighted synthesized beam. (c) CO(4-3) spectra (black lines) and [CII] spectra overlaid (shaded yellow bars) for all 14 sources centred at the biweight cluster redshift $z = 4.304$. The [CII] spectra are scaled down in flux by a factor of ten for clarity of presentation. The red arrows show the velocity offsets determined by fitting a Gaussian profile to the CO(4-3) spectra for all sources except for H, K, L, M, and N, for which we used [CII] because these are not detected in CO(4-3).

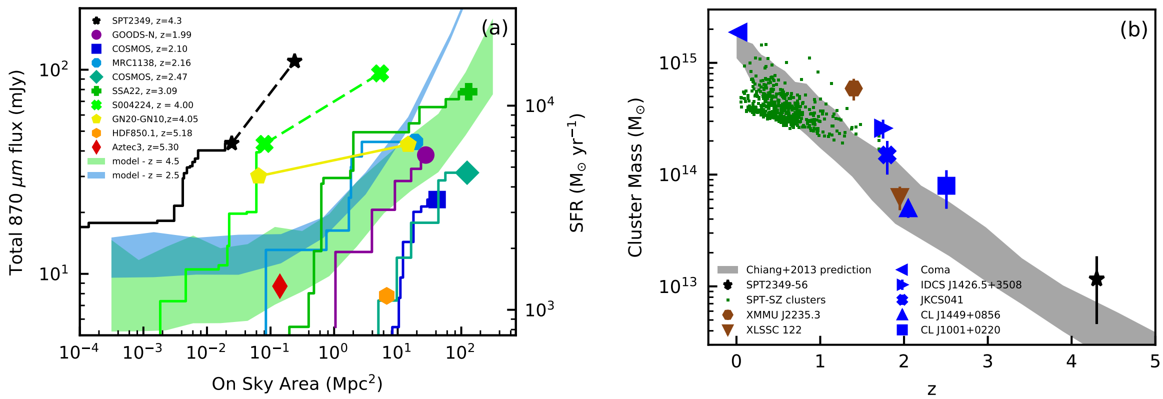

Figure 2: Comparison of SPT2349-56 to other cluster and proto-cluster systems. (a) The cumulative 870-μm flux density vs. on-sky area for SPT2349-56, compared to other SMG-rich overdensities at high redshift (see Methods for details). The solid black line shows the ALMA-identified sources in SPT2349-56, while the dashed line includes the wider-field LABOCA-detected structure. The blue (green) shaded region denotes the maximum flux density vs. area curves obtained in 100 Monte Carlo realizations of a theoretical model for submm-luminous protoclusters at $z = 4.5$ ($z = 2.5$) based on an N-body simulation (see Methods for full details). Most of the literature SMG overdensities are consistent with the model expectations, whereas SPT2349-56 lies vastly above the region spanned by the model. A recently discovered $z = 4$ protocluster from *Herschel*,[24] SMM J004224, is quite a unique system but > 10 times less dense than and likely only $\sim 50\%$ the total luminosity of SPT2349-56. (b) The cluster mass versus redshift is shown for SPT2349-56 and other massive galaxy clusters from the literature with detected ICM and well-defined masses. The colour scheme highlights the different methods for selecting massive clusters employed (brown = X-ray, blue = optical, green = Sunyaev-Zeldovich effect). Error bars represent the 1 σ standard deviation. We also show the mean protocluster most-massive-progenitor mass vs. z relation predicted by N-body simulations.[12] The location of SPT2349-56 in this plane suggests a very massive descendant (halo mass of $> 10^{15}$ $M_{\odot}$ at z = 0), although we caution that the complex growth histories of dark matter halos make it difficult to reliably predict the z = 0 halo mass from the halo mass at a given epoch.[21]

Table 1: Derived physical properties of SPT2349-56 protocluster members.

Source	$\Delta V^{\ddagger}$ [km s^{-1}]	SFR [M$_{\odot}$ yr^{-1}]	$M_{\rm gas}$ [10^{10} M$_{\odot}$]	$M^{\circ}_{\rm dyn}$ [10^{11} M$_{\odot}$]
A	137 ± 35	1170 ± 293	12.0 ± 2.1	11.5 ± 2.7
B	107 ± 31	1227 ± 307	11.2 ± 2.0	8.4 ± 2.0
C	830 ± 12	907 ± 227	6.7 ± 1.2	< 1.4
D	196 ± 40	530 ± 140	8.4 ± 1.5	17.5 ± 4.8
E	312 ± 21	497 ± 141	4.8 ± 0.9	< 2.4
F	623 ± 82	505 ± 128	3.4 ± 0.7	12.4 ± 6.3
G	−74 ± 37	409 ± 103	1.6 ± 0.4	< 1.2
H	−492 ± 28	310 ± 80	4.4 ± 2.0†	4.4 ± 1.1*
I	537 ± 78	268 ± 71	2.2 ± 0.5	< 5.3
J	−251 ± 35	243 ± 67	2.2 ± 0.5	2.3 ± 0.9
K	862 ± 12	208 ± 54	3.1 ± 1.4†	1.5 ± 0.2*
L	−147 ± 18	122 ± 34	3.3 ± 1.5†	2.4 ± 0.5*
M	261 ± 21	75 ± 30	1.2 ± 0.6†	< 0.4 *
N	319 ± 25	64 ± 25	1.0 ± 0.5†	< 0.9 *

° Unresolved sources represent upper limits on the dynamical mass

‡ Velocity offsets relative to z = 4.300

† [CII] line used to derive $M_{\rm gas}$as CO(4-3) is not detected

* [CII] profile used to derive $M_{\rm dyn}$, otherwise CO(4-3) used

Extended Data Table 1: Observed properties of SPT2349-56 protocluster members

Source	RA (J2000) [h:m:s]	Dec (J2000) [d:m:s]	$S_{1090\,\mu\mathrm{m}}$ [mJy]	$S_{870\,\mu\mathrm{m}}$ [mJy]	$S_{3.6\,\mu\mathrm{m}}$ [μJy]	$S_{4.5\,\mu\mathrm{m}}$ [μJy]	CO(4-3) $\int$ S dv [Jy km s^{-1}]	CO(4-3) FWHM [km s^{-1}]	[CII] $\int$ S dv [Jy km s^{-1}]	[CII] FWHM [km s^{-1}]	Size † [kpc]
A	23:49:42.67	−56:38:19.3	4.63 ± 0.04	7.8 ± 0.1	4.3 ± 0.5	5.5 ± 1.3	0.99 ± 0.03	376 ± 46	8.81 ± 0.26	354 ± 30	5.2 × < 2.8
B	23:49:42.79	−56:38:24.0	4.35 ± 0.04	8.2 ± 0.1	6.4 ± 0.3	-	0.92 ± 0.03	341 ± 38	7.53 ± 0.22	314 ± 28	3.2 × 3.1
C	23:49:42.84	−56:38:25.1	2.69 ± 0.04	6.0 ± 0.1	19.6 ± 0.8	18.0 ± 2.8	0.55 ± 0.02	154 ± 13	4.43 ± 0.17	160 ± 10	< 2.8 × < 2.8
D	23:49:41.42	−56:38:22.6	2.20 ± 0.08	3.5 ± 0.3	3.4 ± 0.5	4.8 ± 2.2	0.69 ± 0.04	485 ± 64	3.62 ± 0.78	346 ± 129	4.1 × < 2.8
E	23:49:41.23	−56:38:24.4	2.12 ± 0.11	3.3 ± 0.4	6.8 ± 0.7	7.1 ± 2.1	0.39 ± 0.02	199 ± 23	3.47 ± 1.24	310 ± 137	< 2.8 × < 2.8
F	23:49:42.14	−56:38:25.8	1.69 ± 0.05	3.4 ± 0.1	2.0 ± 0.4	-	0.28 ± 0.03	396 ± 103	4.28 ± 0.35	353 ± 35	4.5 × 2.9
G	23:49:42.74	−56:38:25.1	1.11 ± 0.04	2.7 ± 0.1	1.6 ± 0.4	-	0.14 ± 0.02	147 ± 41	-	-	< 2.8 × < 2.8
H	23:49:43.46	−56:38:26.2	0.85 ± 0.05	2.1 ± 0.1	1.3 ± 0.2	-	-	-	3.63 ± 0.30	236 ± 31	3.9 × 3.7
I	23:49:42.22	−56:38:28.3	0.78 ± 0.05	1.8 ± 0.1	1.2 ± 0.2	-	0.18 ± 0.03	277 ± 90	3.18 ± 0.32	236 ± 24	3.1 × < 2.8
J	23:49:43.22	−56:38:30.1	0.61 ± 0.06	1.6 ± 0.2	4.9 ± 0.5	6.9 ± 2.0	0.19 ± 0.02	151 ± 38	3.79 ± 0.29	138 ± 15	6.8 × 4.1
K	23:49:42.96	−56:38:17.9	0.34 ± 0.04	1.4 ± 0.1	3.6 ± 0.6	5.2 ± 1.6	-	-	2.54 ± 0.17	129 ± 12	5.2 × 4.3
L	23:49:42.38	−56:38:25.8	0.23 ± 0.04	0.8 ± 0.1	3.9 ± 0.5	5.4 ± 1.8	-	-	2.78 ± 0.20	176 ± 20	4.1 × 2.9
M	23:49:43.39	−56:38:21.1	0.21 ± 0.05	0.5 ± 0.2	3.8 ± 0.5	5.1 ± 1.6	-	-	1.04 ± 0.14	87 ± 23	-
N	23:49:43.27	−56:38:22.9	0.18 ± 0.04	0.4 ± 0.1	3.4 ± 0.6	4.6 ± 1.7	-	-	0.86 ± 0.16	128 ± 26	-

† Major and minor axis FWHM source sizes after de-convolution with a 0.5-arcsec Gaussian beam. Sizes are converted from arcsec to kpc assuming an angular diameter distance of 6.9 kpc per arcsec at z = 4.3. The typical uncertainty in the quoted sizes is 1.5 kpc. Sources with a de-convolved size less than 0.4 arcsec (2.8 kpc) are considered unresolved.

Extended Data Table 2: Properties of the 3 ATCA CO(2-1) sources

ATCA source	ALMA ID	$\int$ S dv [Jy km s^{-1}]	σ_V [km s^{-1}]	L′(CO 2-1) 10^{11} [K km s^{-1} pc^2]	M_{gas} [10^{11} M$_\odot$]
Central (C)	B, C, G	0.69 ± 0.076	372 ± 47	1.22 ± 0.12	1.33 ± 0.15
West (W)	D, E	0.16 ± 0.04	166 ± 47	0.29± 0.07	0.32 ± 0.08
North (N)	A, K	0.085 ± 0.0028	175 ± 68	0.15 ± 0.05	0.16 ± 0.05

Extended Data Table 3: Observed properties of all red ($S_{500\,\mu\mathrm{m}} > S_{350\,\mu\mathrm{m}} > S_{250\,\mu m}$) SPIRE sources in the field surrounding SPT2349-56. The LABOCA sources corresponding to SPT2349-56 are listed first, and the red SPIRE sources in the surrounding field follow. All sources listed are highlighted in Extended Data Figure 5.

RA (J2000) [h:m:s]	Dec (J2000) [d:m:s]	$S_{250\,\mu m}$ [mJy]	$S_{350\,\mu m}$ [mJy]	$S_{500\,\mu m}$ [mJy]	$S_{850\,\mu m}$ [mJy]	d[†] [arcmin]
23:49:42	−56:38:25	45 ± 3	71 ± 3	96 ± 3	77.0 ± 2.9	-
23:49:43	−56:37:31	21 ± 3	37 ± 3	43 ± 3	25.0 ± 2.8	0.9
23:49:25	−56:35:27	23 ± 4	26 ± 4	32 ± 4	2.9 ± 1.7	5.2
23:49:39	−56:36:33	12 ± 3	16 ± 3	23 ± 4	3.9 ± 1.3	2.1
23:49:36	−56:41:17	7 ± 3	14 ± 3	19 ± 3	3.2± 1.6	3.2
23:49:55	−56:34:17	6 ± 4	10 ± 3	20 ± 5	4.8 ± 1.8	5.3
23:49:12	−56:40:31	11 ± 5	16 ± 5	22 ± 5	6.8 ± 2.6	7.7

[†] Distance from central SPT2349-56 source.

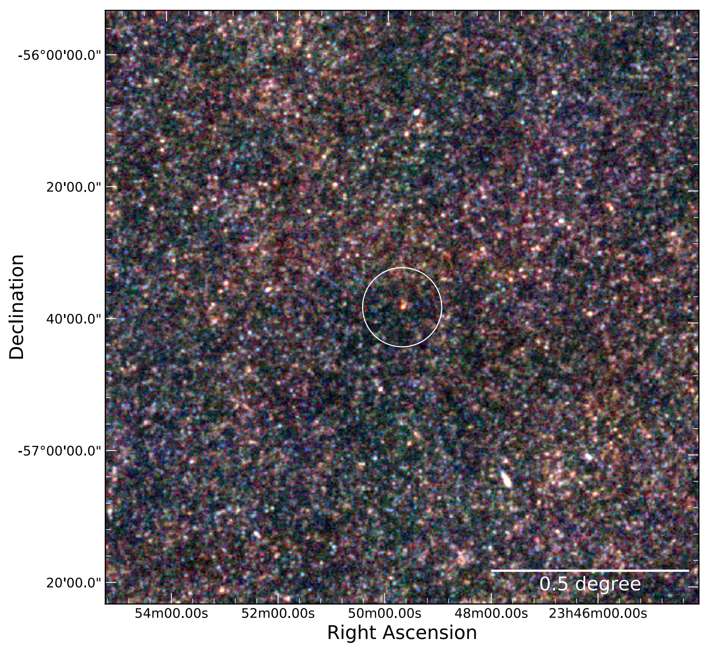

Extended Data Figure 1: ***Herschel*-SPIRE image.** A RGB scale is used to represent 500, 350, and 250 μm, with the red SPT2349-56 extended complex clearly visible in a relative void in the foreground $z \sim 1$ cosmic infrared background (blue to green-coloured galaxies).

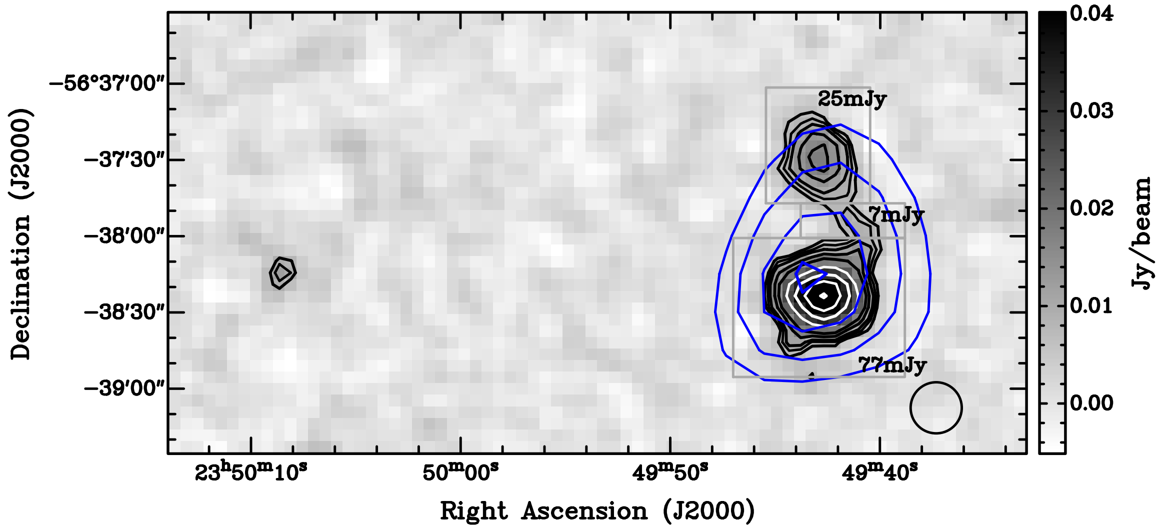

Extended Data Figure 2: Wide field 870-μm image and photometry. A wide-field LABOCA image (21″ beam size) of SPT2349-56. The image rms noise is 1.3 mJy at center, increasing to 2mJy at the edges of the region shown. The total flux density recovered is 110.0±9.5 mJy. Sub-apertures are drawn showing three different regions and their recovered flux densities. SPT 1.4-mm contours are also shown (blue), revealing that even with the 1′ beam of SPT, SPT2349-56 is resolved. One additional submm source is detected at $> 5\sigma$ in the LABOCA image to the east of the primary source, though *Herschel*-SPIRE photometry indicates that it is unlikely to be at $z \sim 4$.

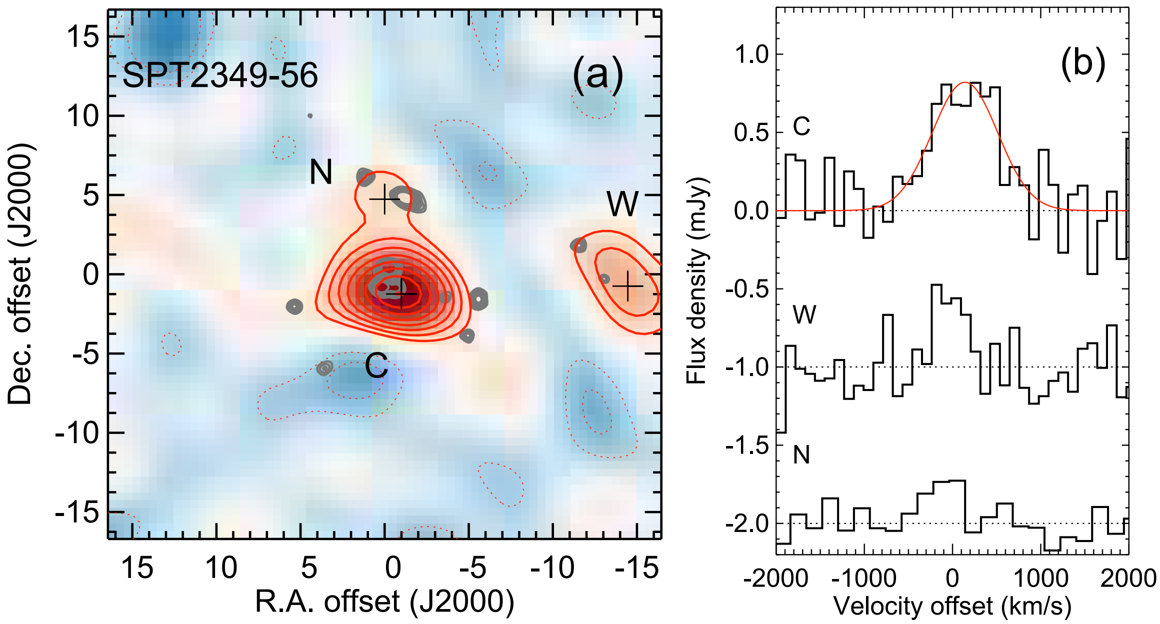

Extended Data Figure 3: CO(2-1) observations of SPT2349-56. (a): The colormap and red contours trace the CO(2-1) line integrated over the central 830 $\mathrm{km\,s^{-1}}$, with contours spaced by 3σ starting at 3σ. The grey contours show the 1.1-mm ALMA continuum detections. (b): One-dimensional spectra extracted at the positions indicated in (a).

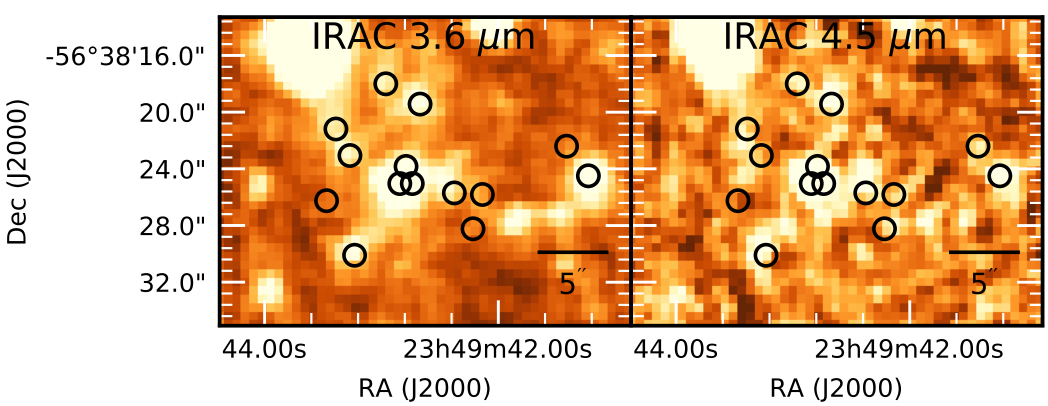

Extended Data Figure 4: IRAC observations of SPT2349-56. Circles display the location of the 14 sources detected in ALMA band 7 described above. Nine sources are detected with IRAC, including the two faintest [CII] sources from the blind line survey.

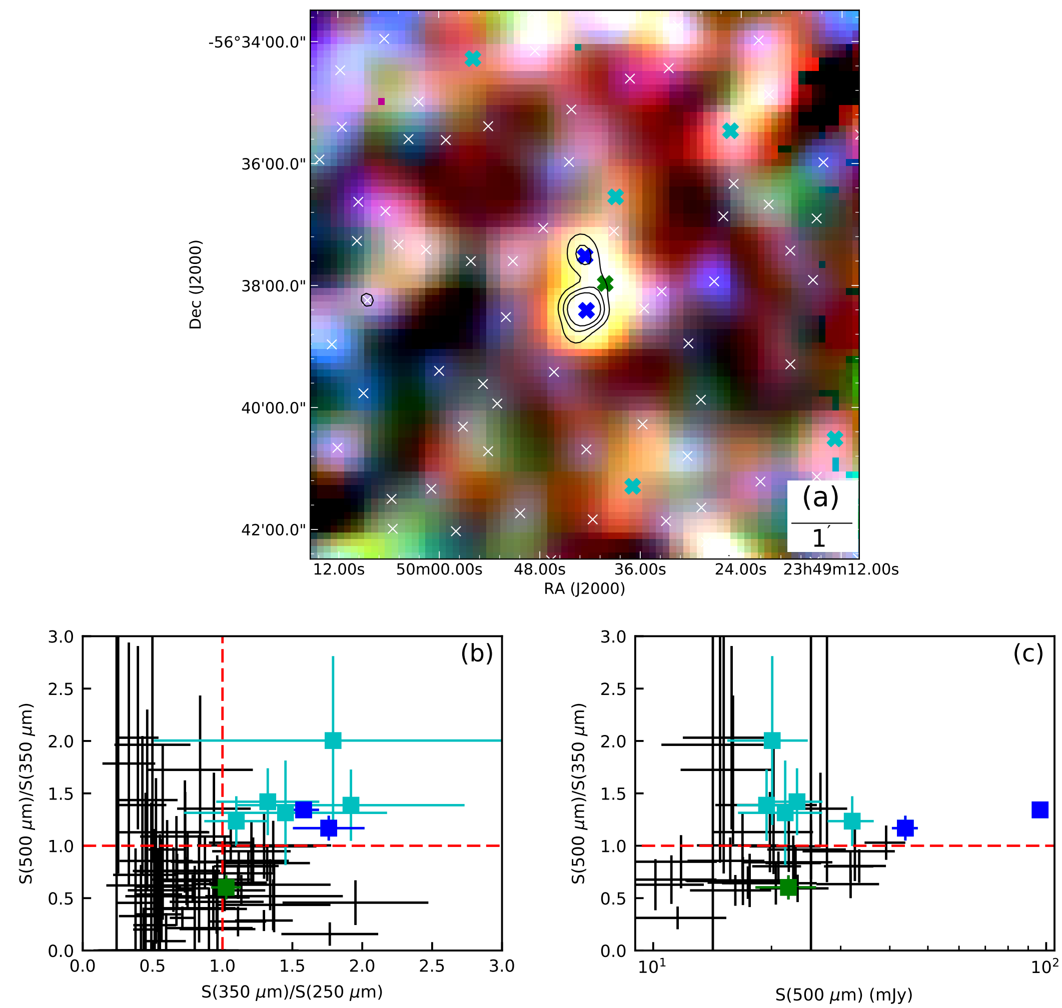

Extended Data Figure 5: SPIRE RGB image and source colours in field surrounding SPT2349-56. (a) Deep SPIRE false colour image is shown with LABOCA contours overlaid. Locations of 250-μm peaks used for analysis are marked with crosses (the faintest are not visible because of the contrast adopted in the image). Colour-colour (CC, (b)) and colour-flux (CF, (c)) diagrams for 250 μm sources are also shown. Error bars represent the 1 σ standard deviation. The CC diagram shows sources with SNR(250 μm)>3 and is dominated by the $z \sim 1$ cosmic infrared background in the *foreground* of SPT2349-56 (sources with colours ranging from blue to green). The CF diagram applies an additional SNR(500 μm)>3 cut. The CC and CF diagrams show that one of three peaks associated with SPT2349-56 is likely a lower-redshift interloper (green symbol), but also that there are five additional sources (blue symbols) in the surrounding 2 Mpc region with colours ($S_{500\,\mu\mathrm{m}} > S_{350\,\mu\mathrm{m}} > S_{250\,\mu\mathrm{m}}$) that are suggestive of z=4.3.

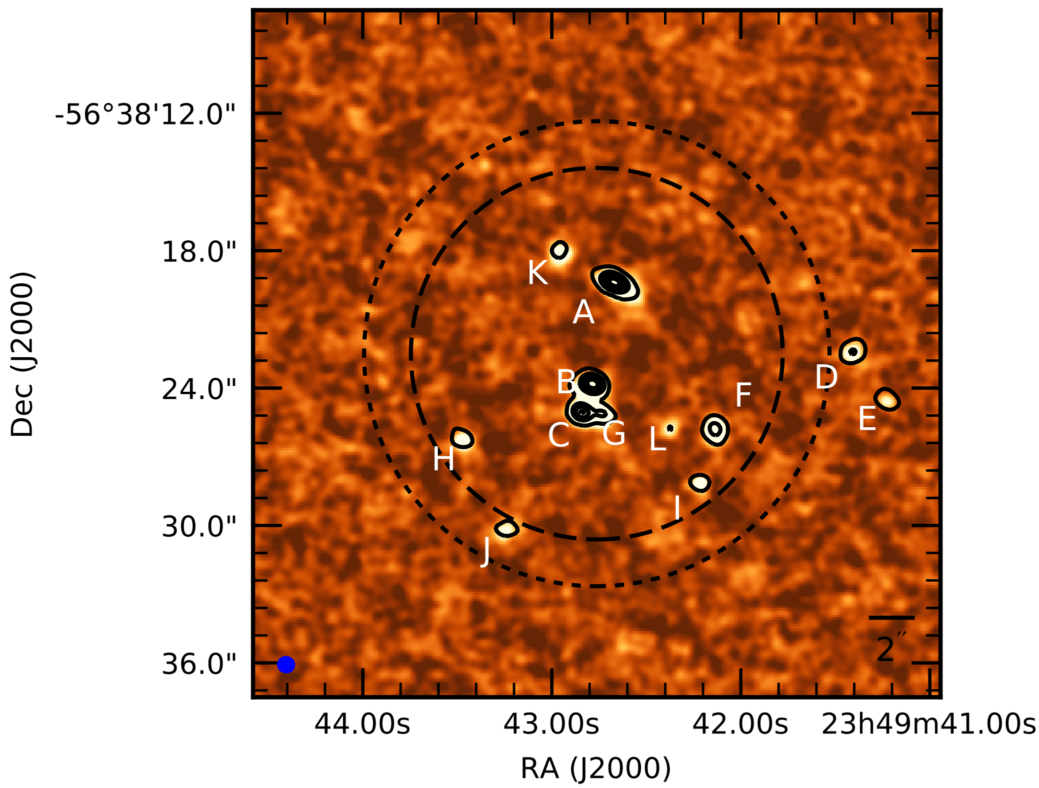

Extended Data Figure 6: Line-free 870-μm continuum image. Contours represent 1090 μm and begin at 0.15 mJy (SNR$\sim$ 5) and increase in steps of 2 mJy. The half-power beam widths are also shown for the 870-μm observations (long dashed line – 18″) and 1.1-mm observations (short dashed line – 23″). We find good agreement between the two wavelengths, with all sources A-L detected in both images. Note that neither the 870-μm image nor the 1090-μm contours are corrected for the primary beam, thus sources away from the center, especially D & E, appear fainter than they are intrinsically.

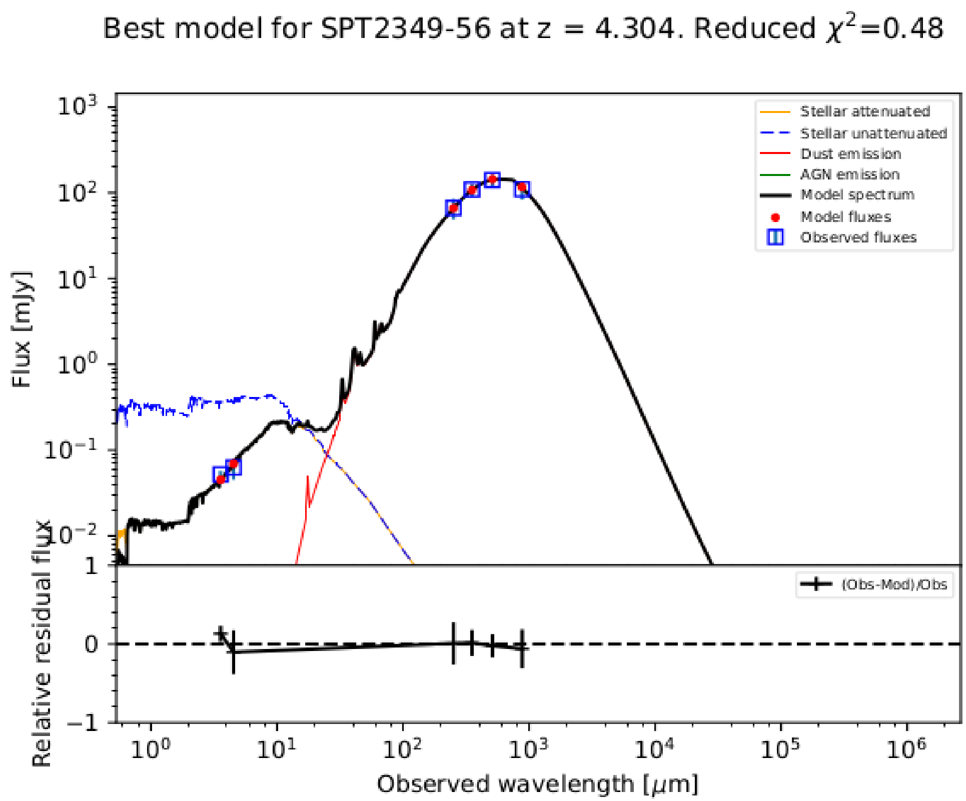

Extended Data Figure 7: Spectral energy distribution of SPT2349-56. The SED of the extended SPT2349-56 source is shown, including the summed deconvolved *Herschel*-SPIRE flux densities, the total 870-μm LABOCA flux density, and the summed IRAC flux densities. We do not include the SPT 1.4, 2.0, and 3.0 mm points because the source is elongated and flux measurements are difficult with the filtering used to make the map. Fitting the SED yields an IR luminosity of $(8.0 \pm 1.0) \times 10^{13}$ $L_\odot$.